Efficient Registration of Non-rigid 3-D Bodies

Huizhong Chen, *Student Member, IEEE* and Nick Kingsbury, *Member, IEEE*

Abstract

We present a novel method to perform accurate registration of 3-D non-rigid bodies, by using phase-shift properties of the dual-tree complex wavelet transform (DT-$\mathbb{C}$WT). Since the phases of DT-$\mathbb{C}$WT coefficients change approximately linearly with the amount of feature displacement in the spatial domain, motion can be estimated using the phase information from these coefficients. The motion estimation is performed iteratively, firstly by using coarser level complex coefficients to determine large motion components and then by employing finer level coefficients to refine the motion field. We use a parametric affine model to describe the motion, where the affine parameters are found locally by substituting into an optical flow model and solving the resulting over-determined set of equations. From the estimated affine parameters, the motion field between the sensed and the reference datasets can be generated and the sensed dataset can then be spatially shifted and interpolated to align with the reference dataset.

Index Terms

Image registration, dual-tree complex wavelet transform, optical flow.

EDICS Category: ARS-IVA, TEC-MRS

I. INTRODUCTION

With the increasing availability of 3-D imaging systems like Computed Tomography (CT) and Magnetic Resonance Imaging (MRI), multidimensional image analysis has become a key topic for research. In most image processing tasks which involve combining data from multiple sources, accurate estimation of motion between datasets is of great importance. The objective of image registration is geometrically to align multiple images of a similar scene, acquired at different times and positions and with different

Huizhong Chen is with the Department of Electrical Engineering, Stanford University, US. Nick Kingsbury is with the Department of Engineering, University of Cambridge, UK. Email: hchen2@stanford.edu, ngk@eng.cam.ac.uk
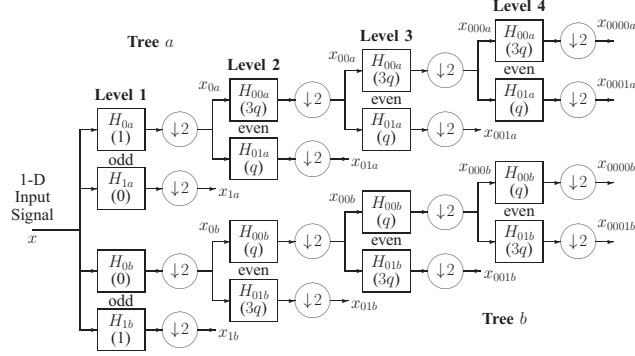
Fig. 1. Dual tree of real filters for the Q-shift CWT, giving real and imaginary parts of complex coefficients from tree a and tree b respectively. Figures in brackets indicate the approximate delay for each filter, where $q = \frac{1}{4}$ sample period. (Adapted from [1])

imaging devices. Registration is widely used in many applications, such as medical imaging (aligning datasets for disease diagnosis and treatment planning), computer vision (object tracking, structure-from-motion), and remote sensing (change detection, mosaicing, image fusion, super resolution). In this paper, we mainly consider applying the registration algorithm to medical images. Medical image registration differs from other 3-D object registrations in three main aspects: 1) images of a medical object can change significantly with time due to elastic tissue structures or in the presence of abnormalities. 2) medical image registration tends to focus on internal object structures. 3) accurate registration must be achieved for optimal diagnosis. However, it should be noted that our algorithm does not make assumptions about specific types of image data, so the proposed method can be generalized to other image categories.

Three-dimensional motion estimation has been studied for some time but improved computation and memory resources now make higher performance methods increasingly feasible. In 3-D registration, motion can occur along all 3 dimensions so it is suboptimal to register datasets slice by slice. Also, for non-rigid objects such as human tissue, the movement is typically non-uniform throughout the dataset and hence the motion should be described locally, rather than just globally. Further, the object of interest may have experienced changes in the sensed and the reference datasets, e.g., the removal of tumor in medical images before and after a clinical intervention. Hence a good multidimensional registration algorithm should be accurate, robust and computationally efficient.

Previous work on image registration can be broadly classified into feature-based methods and area-based methods. Feature-based approaches extract salient features from the sensed and the reference datasets, and aim to find the transformation which minimizes the distance between corresponding features. The extracted features can be regions, edges or interest points. Matas et al. [2] detect Maximally

Stable Extremal Regions and setup the correspondence between pairs of images based on these stable regions. Li et al. [3] proposed a contour-based method which use region boundaries and other strong edges as matching primitives. In [4], Takacs et al. use FAST (Features from Accelerated Segment Test) keypoints [5] and perform descriptor matching to estimate the image transformation. Ta et al. [6] proposed SURFTrac which matches Hessian interest points inside a 3-D image pyramid. In contrast to feature-based methods, area-based methods attempt to perform registration without extracting salient features. Common area-based approaches include cross-correlation (CC) methods and mutual information (MI) methods. For CC methods like the algorithms described in [7], [8], a displacement vector is computed over pairs of tiles in the sensed and the reference images by maximizing the normalized CC. Another type of registration technique that is closely related to the CC methods is the sequential similarity detection algorithm, which maximizes the sum of absolute differences of the image intensity [9]. Image registration with MI was first proposed by Viola and Wells [10] and Maes and Collignon [11], where the registration is done by optimizing the MI between pairs of datasets. Thevenaz et al. [12] employed Parzen windows to compute the joint probability histogram and developed an MI optimizer with the Marquardt-Levenberg method for multimodal image registration. In [13], the joint probability was approximated by discrete histograms and the maximization of MI was achieved by a multiresolution hill climbing algorithm. For a more complete review on image registration methods, readers are referred to [14]–[19].

Our non-rigid body registration algorithm is based on the ideas of Hemmendorff [20], [21] with significant changes designed to improve computational efficiency. In particular, the dual-tree complex wavelet transform (DT-$\mathbb{C}$WT) [1], [22] is used as the front-end filter bank to take advantage of its near shift-invariance and directional selectivity, combined with relatively low redundancy and computation load. The algorithm is fully automated and may be applied to estimate motion for a wide range of non-rigid objects. In addition, since the motion of a rigid body is just a special case of non-rigid motion, our proposed motion registration method can also be used to register rigid objects, although difficulties may arise at sharp motion boundaries due to the spatial support regions of the filters used. Finally, our image registration algorithm is based on aligning the phases of the DT-$\mathbb{C}$WT coefficients, which are robust to local mean and contrast changes of the two datasets being registered. The proposed algorithm is well suited to medical data where any large motion is mainly global, and smaller local relative motions can be obtained from the finer resolution motion estimation in later stages of the algorithm. To handle very large local motion, an extension of our method is to perform motion estimation by searching over adjacent regions where the local motion has occurred.
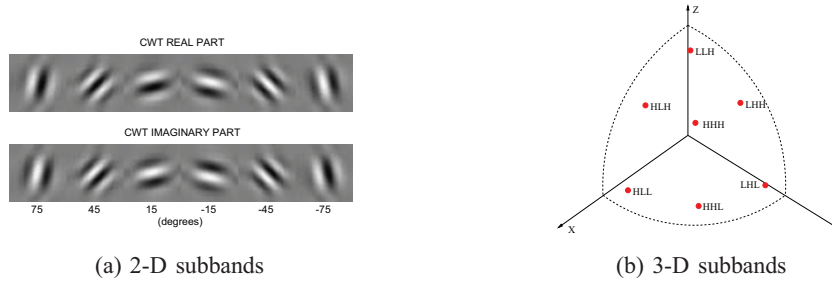
(a) 2-D subbands   (b) 3-D subbands

Fig. 2. (a) The impulse responses of the 2-D DT-ℂWT subbands at level 4, in the order HL, HH, LH, L*H, H*H, H*L. The filtering is performed on rows first and then on columns, e.g. LH means low-pass filtering on rows followed by high-pass filtering on columns. (b) The orientation of 3-D DT-ℂWT subbands on one quadrant of a hemisphere. The filtering is performed in the sequence: rows, columns and slices.

II. DUAL-TREE COMPLEX WAVELET TRANSFORM

This section contains a brief introduction to the DT-ℂWT and its properties for image registration. The DT-ℂWT in 3-D will be discussed in some detail since we focus on registering 3-D datasets.

A. The DT-ℂWT and its properties

The DT-ℂWT is an enhancement of the conventional discrete wavelet transform (DWT), with two distinctive properties: near shift-invariance and directional selectivity in 2-D or higher dimensions [23]. The basic idea of the DT-ℂWT is to employ a Hilbert pair of real DWTs in parallel [22] to produce the real and imaginary parts of complex wavelet coefficients. Its framework for 1-D signals is shown in Fig.1.

The near shift-invariance property of the DT-ℂWT means that the impulse response of a given subband from the transform input to the inverse-transform output is approximately independent of shift and hence free of aliasing [1]. Simoncelli et al. [24] showed that shift invariance is equivalent to interpolability of the subband coefficients. Hence for image registration purposes, the DT-ℂWT coefficients from each subband can be interpolated to represent the transformation of shifted signals in the spatial domain.

The 1-D DT-ℂWT can be extended to 2-D to produce directionally selective wavelet subbands [22], [23], as shown in Fig.2a. The impulse responses of the oriented wavelet filters are important for motion estimation, because the motion in the direction normal to the stripes of the filter response will cause an approximately linear phase change in the corresponding subband coefficients. In other words, the DT-ℂWT has an analogy to the Fourier transform, in the way that a shift in the spatial domain corresponds to a linear phase change in the frequency domain. For the DT-ℂWT in 3-D, each transform level has 28
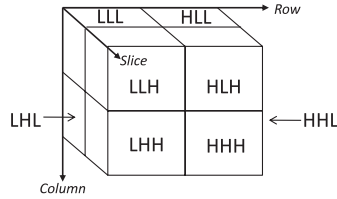
Fig. 3. The 8-band structure of 3-D DT-ℂWT, where each cube represents a subband of one of the eight DWTs in a DT-ℂWT. The filtering is performed in the sequence of rows, columns and slices. E.g. HLL means high-pass filtering on rows and low-pass filtering on columns and slices.

subbands which are selective to near-planar surfaces. The orientations of these surfaces for the 28 subbands correspond to approximately equally spaced patches on the surface of a hemisphere, one quadrant of which is shown in Fig.2b.

The bandwidths of the wavelet filters are approximately one octave wide, which are well suited to detection of edges (2-D) or surfaces (3-D) since they are wide enough in frequency to be well localized in space, and yet narrow enough for their responses to approximate modulated waves with linear phase-versus-displacement characteristics. At any one scale, they approximately uniformly tile the 2-D frequency plane or 3-D frequency volume. Hence we feel they are close to optimal in their characteristics.

B. The DT-ℂWT in 3-D

The DT-ℂWT is implemented in 3-D by performing separable filtering on rows, columns and slices of the 3-D dataset. This filtering process produces the structure shown in Fig.3, which contains 8 bands, namely LLL, HLL, LHL, HHL, LLH, HLH, LHH and HHH, as found in a conventional 3-D DWT. But in the dual-tree version, since there are two trees of filtering on each dimension, the DT-ℂWT produces an octal-tree system which introduces a redundancy of 2:1 on each dimension and gives a total redundancy of 8:1 in 3-D.

Each subband in the octal-tree system produces 8 real coefficients (one from each tree) at each spatial location, and these can yield 4 directional subbands of complex coefficients by simple arithmetic sum and difference operations [22]. Because of the Hilbert pair relationships, these 4 subbands correspond to different quadrants of the 3-D spectral half-space, as depicted in Fig.4. Since the LLL band is used for the next level of complex wavelet transform, there are altogether $(8-1) \times 4 = 28$ directional subbands for each DT-ℂWT level. These subbands are produced by all the bands from the 8-band stucture except for the LLL band. To see how a quad of directional subbands can be generated by the coefficients of one

band of the 8-band structure, we specifically consider the HHH band at a certain level of the DT-$\mathbb{C}$WT (other bands follow the same derivation). The 3-D wavelet for the 1st quadrant HHH subband can be written as:

$$\psi_1(x,y,z) = [\psi_a(x) + j\psi_b(x)][\psi_a(y) + j\psi_b(y)][\psi_a(z)$$
$$+ j\psi_b(z)] \tag{1}$$
$$= [\psi_a(x)\psi_a(y)\psi_a(z) - \psi_b(x)\psi_b(y)\psi_a(z)$$
$$- \psi_a(x)\psi_b(y)\psi_b(z) - \psi_b(x)\psi_a(y)\psi_b(z)]$$
$$+ j[\psi_a(x)\psi_a(y)\psi_b(z) - \psi_b(x)\psi_b(y)\psi_b(z)$$
$$+ \psi_a(x)\psi_b(y)\psi_a(z) + \psi_b(x)\psi_a(y)\psi_a(z)] \tag{2}$$

The subscripts a and b in the above equations denote tree a (generating the real part) and tree b (generating the imaginary part) in Fig.1. In (2), $\psi_a(i)$ and $\psi_b(i)$ are the tree a and tree b high-pass filters being applied to dimension $i \in \{x,y,z\}$, with x, y and z denoting the axes of row, column and slice respectively. Note that the 1-D DT-$\mathbb{C}$WT filters suppress the negative half of the frequency spectrum. Therefore the wavelet in (2) only represents the spectrum in the 1st quadrant of the upper half of the frequency domain. However, real 3-D datasets contain independent frequency components in the 1st, 2nd, 3rd and 4th quadrants of the upper-half frequency space, as depicted in Fig.4. The wavelets for the 2nd, 3rd and 4th quadrants can be obtained from the following equations:

$$\psi_2(x,y,z) = [\psi_a(x) - j\psi_b(x)][\psi_a(y) + j\psi_b(y)][\psi_a(z)$$
$$+ j\psi_b(z)] \tag{3}$$
$$\psi_3(x,y,z) = [\psi_a(x) + j\psi_b(x)][\psi_a(y) - j\psi_b(y)][\psi_a(z)$$
$$+ j\psi_b(z)] \tag{4}$$
$$\psi_4(x,y,z) = [\psi_a(x) - j\psi_b(x)][\psi_a(y) - j\psi_b(y)][\psi_a(z)$$
$$+ j\psi_b(z)] \tag{5}$$

It can be seen that $\psi_2(x,y,z)$, $\psi_3(x,y,z)$ and $\psi_4(x,y,z)$ can be easily obtained by arithmetic sum and difference operations on the terms of $\psi_1(x,y,z)$ in (2). If we rewrite (2) as

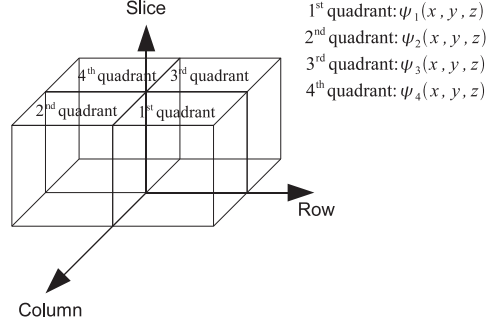$$\psi_1(x,y,z) = [A - G - D - F] + j[B - H + C + E] \tag{6}$$

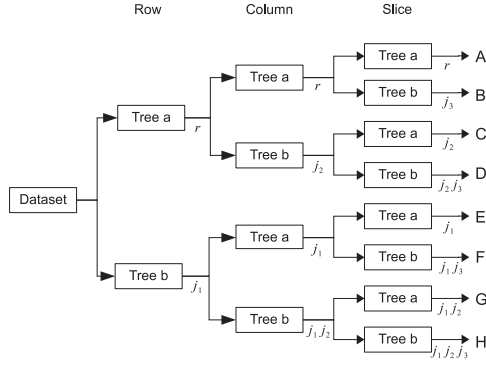Fig. 4. The upper half-space of the frequency spectrum of 3-D datasets.

Fig. 5. For each of the row, column and slice dimensions, high-pass or low-pass filters are applied to generate the corresponding octal-tree components. r means a real component, while j_1, j_2 and j_3 denote the imaginary operator j for the row, column and slice directions respectively. For components in the 1st quadrant, $j_1 = +j$, $j_2 = +j$ and $j_3 = +j$; for the 2nd quadrant, $j_1 = -j$, $j_2 = +j$ and $j_3 = +j$; for the 3rd quadrant, $j_1 = +j$, $j_2 = -j$ and $j_3 = +j$; for the 4th quadrant, $j_1 = -j$, $j_2 = -j$ and $j_3 = +j$.

where the symbols A to H represent the components in (2) in the same order. Then $\psi_2(x, y, z)$, $\psi_3(x, y, z)$ and $\psi_4(x, y, z)$ in (3), (4) and (5) can be rewritten as:

$$\psi_2(x,y,z) = [A - G + D + F] + j[-B + H + C + E] \tag{7}$$

$$\psi_3(x,y,z) = [A + G + D - F] + j[B + H - C + E] \tag{8}$$

$$\psi_4(x,y,z) = [A + G - D + F] + j[-B - H - C + E] \tag{9}$$

Fig.5 illustrates how the components of the octal-tree system in equations (6), (7), (8) and (9) are produced. The outputs A to H in Fig.5 have the same meaning as in the equations.

C. Memory considerations for the 3-D DT-$\mathbb{C}$WT

The redundancy of the 3-D DT-$\mathbb{C}$WT is 8:1, which, although modest for a shift-invariant 3-D transform, still tends to cause heavy computation and large memory usage, compared with a non-redundant transform. To solve this problem, our algorithm only keeps the LLL band of the DT-$\mathbb{C}$WT at level 1 and all other level 1 bands are discarded. In this way, the redundancy is eliminated, giving a 1:1 transform. Note that although all high-pass bands at level 1 are ignored, this does not cause excessive loss of information, because typical real-world datasets do not have very sharp edges and the highest frequency components are largely dominated by noise. Also, the level-1 wavelets have poorer linear phase-shift properties than at coarser levels, and so are less useful for registration.

III. OVERVIEW OF MOTION ESTIMATION

A. Description of motion: the affine model

Each motion vector is in the direction of the displacement, with amplitude equal to the amount of shift. For non-rigid registration purposes, the motion vectors should be described locally. The full set of motion vectors which contains the motion of the dataset at every location is called the motion field.

In this work, we describe the 3-D motion field by the affine transform [25], which can model typical motions like translation, rotation, scaling and shear. A major advantage of using the affine model lies in the fact that if the motions at two locations are from the same affine model (e.g. shift, rotation, scaling or shear, typically belonging to the same object) then their affine parameters should also be the same. This property is important when overcoming the problems of ill-conditioning due to limited aperture (known as the aperture problem [26]), for estimating motions of rigid bodies (section V-A) and smoothing the motion estimates across a region of the dataset (section IV-E).

B. Theoretical background of motion estimation

The model described here is based on the parametric model introduced by Hemmendorff [21], with significant changes in order to take full advantage of the efficient DT-$\mathbb{C}$WT front end.

1) The motion constraint: We define the 4-element homogeneous displacement vector at location $\mathbf{x}$ to be:

$$\tilde{\mathbf{v}}(\mathbf{x}) = \begin{bmatrix} \mathbf{v}(\mathbf{x}) \\ 1 \end{bmatrix} \tag{10}$$

where $\mathbf{v}(\mathbf{x})$ is the motion vector at location $\mathbf{x} = [x, y, z]^T$. A motion constraint vector is a 4-element vector $\mathbf{c}(\mathbf{x})$ that defines a plane in 3-D space and satisfies:

$$\mathbf{c}^{\mathrm{T}}(\mathbf{x})\,\tilde{\mathbf{v}}(\mathbf{x}) = 0 \tag{11}$$

Horn and Schunk in [27] showed that the motion constraints can be estimated as the spatiotemporal gradient of the image intensity. This is known as the optical flow model. In the context of 3-D DT-$\mathbb{C}$WT, since the phase of each complex coefficient has an approximately linear relationship with the local shift vector $\mathbf{v}(\mathbf{x})$, we have the following equation:

$$\frac{\partial \theta_d}{\partial t} = \nabla_{\mathbf{x}}\theta_d \cdot \mathbf{v}(\mathbf{x}) \quad \text{which gives} \quad \begin{bmatrix} \nabla_{\mathbf{x}}\theta_d \\ -\frac{\partial \theta_d}{\partial t} \end{bmatrix}^{\mathrm{T}} \tilde{\mathbf{v}}(\mathbf{x}) = 0 \tag{12}$$

where $\nabla_{\mathbf{x}}\theta_d = \begin{bmatrix} \frac{\partial \theta_d}{\partial x} & \frac{\partial \theta_d}{\partial y} & \frac{\partial \theta_d}{\partial z} \end{bmatrix}^T$, representing the phase gradient at $\mathbf{x}$ for subband d in the directions of x, y and z. Note that d predominantly indexes the different directions of subbands at a particular scale, but it may also index different subband scales too. The term $\frac{\partial \theta_d}{\partial t}$ is the phase gradient between the two datasets being registered, i.e. the phase change at $\mathbf{x}$ of the DT-$\mathbb{C}$WT coefficients of subband d between the two datasets. Comparing (11) and (12), it is clear that the motion constraint vector satisfies the expression:

$$\mathbf{c}_d(\mathbf{x}) = C_d(\mathbf{x}) \begin{bmatrix} \nabla_{\mathbf{x}}\theta_d \\ -\frac{\partial \theta_d}{\partial t} \end{bmatrix} \tag{13}$$

where $C_d(\mathbf{x})$ is a scalar weighting factor which can be designed to reflect the confidence of the motion constraint at $\mathbf{x}$ in the direction of subband d. In applications where the two datasets being registered are not identical, it is desirable to give a larger weight to locations containing similar features and a smaller weight to locations with inconsistent features between the two datasets. These inconsistent features may be caused by the need to improve the image visibility (injection of radiocontrast agents as shown in Fig.9), the actual development of disease (removal of tumor as shown in Fig.10), or image noise. In order to limit the motion estimation outliers caused by the inconsistent features, we design the confidence measure $C_d(\mathbf{x})$ defined by the following expression, which gives highest weight to consistent features and lower weight to less consistent features:

$$C_d(\mathbf{x}) = \frac{|\sum_{k=1}^{8} u_k^* v_k|^2}{\sum_{k=1}^{8}(|u_k|^3 + |v_k|^3) + \varepsilon} \tag{14}$$

where u_k and v_k are the wavelet coefficients in the reference and the sensed dataset respectively, and the subscripts $k = 1 \ldots 8$ denote the 8 neighboring wavelet coefficients which are on a cube centered at

location $\mathbf{x}$ in subband d. The small positive constant ε prevents the denominator from going to zero if the wavelet coefficients become very small. It should be comparable with the cube of the expected amplitude of the measurement noise. Note that the numerator in (14) is proportional to the fourth power of the coefficient amplitudes, while the denominator is proportional to their cubes (ignoring ε), so overall C_d varies linearly with amplitude, which naturally gives greater weight to stronger features in the dataset.

2) The cost function: The affine model equation is written as:

$$\mathbf{v}(\mathbf{x}) = \begin{bmatrix} 1 & 0 & 0 & x & 0 & 0 & y & 0 & 0 & z & 0 & 0 \\ 0 & 1 & 0 & 0 & x & 0 & 0 & y & 0 & 0 & z & 0 \\ 0 & 0 & 1 & 0 & 0 & x & 0 & 0 & y & 0 & 0 & z \end{bmatrix} \begin{bmatrix} a_1 \\ \vdots \\ a_{12} \end{bmatrix}$$

$$= \mathbf{K}(\mathbf{x}) \; \mathbf{a} \tag{15}$$

Defining $\tilde{\mathbf{K}}(\mathbf{x}) = \begin{bmatrix} \mathbf{K}(\mathbf{x}) & \mathbf{0} \\ \mathbf{0} & 1 \end{bmatrix}$ and $\tilde{\mathbf{a}} = \begin{bmatrix} \mathbf{a} \\ 1 \end{bmatrix}$, and then using (10), the homogeneous motion vector is given by

$$\tilde{\mathbf{v}}(\mathbf{x}) = \tilde{\mathbf{K}}(\mathbf{x}) \; \tilde{\mathbf{a}} \tag{16}$$

Combining (11) and (16) for all 28 subband directions, we have:

$$\mathbf{c}_d(\mathbf{x})^{\mathrm{T}} \; \tilde{\mathbf{K}}(\mathbf{x}) \; \tilde{\mathbf{a}} = 0 \quad \text{for} \quad d = 1 \ldots 28 \tag{17}$$

Thus for each location $\mathbf{x}$, there are 28 constraint equations, which is an over-determined set for the 12 unknown affine parameters in $\tilde{\mathbf{a}}$. Hence we find the value of $\tilde{\mathbf{a}}$ which minimizes the squared error $\epsilon(\mathbf{x})$. $\epsilon(\mathbf{x})$ is the cost function of our algorithm, given by

$$\epsilon(\mathbf{x}) = \sum_{d=1}^{28} \| \; \mathbf{c}_d^{\mathrm{T}}(\mathbf{x}) \; \tilde{\mathbf{K}}(\mathbf{x}) \; \tilde{\mathbf{a}} \; \|^2$$

$$= \sum_{d=1}^{28} \tilde{\mathbf{a}}^{\mathrm{T}} \; \tilde{\mathbf{K}}^{\mathrm{T}}(\mathbf{x}) \; \mathbf{c}_d(\mathbf{x}) \; \mathbf{c}_d^{\mathrm{T}}(\mathbf{x}) \; \tilde{\mathbf{K}}(\mathbf{x}) \; \tilde{\mathbf{a}}$$

$$= \tilde{\mathbf{a}}^{\mathrm{T}} \; \tilde{\mathbf{Q}}(\mathbf{x}) \; \tilde{\mathbf{a}} \tag{18}$$

where

$$\tilde{\mathbf{Q}}(\mathbf{x}) = \sum_{d=1}^{28} \tilde{\mathbf{K}}^{\mathrm{T}}(\mathbf{x}) \; \mathbf{c}_d(\mathbf{x}) \; \mathbf{c}_d^{\mathrm{T}}(\mathbf{x}) \; \tilde{\mathbf{K}}(\mathbf{x}) \tag{19}$$

In practice, in order to handle the registration of dissimilar image features as well as dealing with the aperture problem, it is often helpful to combine the $\tilde{\mathbf{Q}}(\mathbf{x})$ matrices across more than one level of the

DT-$\mathbb{C}$WT and over a slightly wider area within each level to produce the most accurate estimate of the affine parameters. We therefore define a locality χ to represent this wider spatial and interscale region, such that

$$\tilde{\mathbf{Q}}_\chi = \sum_{\mathbf{x} \in \chi} \tilde{\mathbf{Q}}(\mathbf{x}) \tag{20}$$

The $\tilde{\mathbf{Q}}$ matrices are symmetric and so $\tilde{\mathbf{Q}}_\chi$ can be written in the form:

$$\tilde{\mathbf{Q}}_\chi = \begin{bmatrix} \mathbf{Q}_\chi & \mathbf{q}_\chi \\ \mathbf{q}_\chi^{\mathrm{T}} & q_{0,\chi} \end{bmatrix} \tag{21}$$

where $\mathbf{q}_\chi$ is a 12-element vector and $q_{0,\chi}$ is a scalar.

Substituting (21) into (18) and (20) , the cost function is thus expressed as:

$$
\begin{aligned}
\epsilon_\chi = \sum_{\mathbf{x} \in \chi} \epsilon(\mathbf{x}) &= \tilde{\mathbf{a}}^{\mathrm{T}} \, \tilde{\mathbf{Q}}_\chi \, \tilde{\mathbf{a}} \\
&= \begin{bmatrix} \mathbf{a}^{\mathrm{T}} & 1 \end{bmatrix} \begin{bmatrix} \mathbf{Q}_\chi & \mathbf{q}_\chi \\ \mathbf{q}_\chi^{\mathrm{T}} & q_{0,\chi} \end{bmatrix} \begin{bmatrix} \mathbf{a} \\ 1 \end{bmatrix} \\
&= \mathbf{a}^{\mathrm{T}} \mathbf{Q}_\chi \mathbf{a} + 2 \mathbf{a}^{\mathrm{T}} \mathbf{q}_\chi + q_{0,\chi}
\end{aligned}
\tag{22}
$$

To minimize ϵ_χ, we differentiate the expression of ϵ_χ with respect to $\mathbf{a}$ and set the derivative to zero. Hence

$$\nabla_{\mathbf{a}} \epsilon_\chi = 2 \mathbf{Q}_\chi \mathbf{a} + 2 \mathbf{q}_\chi = 0 \tag{23}$$

and the local affine parameter vector which gives the least squared error is:

$$\mathbf{a}_\chi = -\mathbf{Q}_\chi^{-1} \mathbf{q}_\chi \tag{24}$$

Once the affine parameters have been obtained, the corresponding motion is obtained by substituting the elements of $\mathbf{a}_\chi$ into (15).

IV. THE IMAGE REGISTRATION ALGORITHM

There are three major steps in our registration algorithm: (1) transform the data to the DT-$\mathbb{C}$WT domain; (2) perform motion estimation; (3) register the sensed dataset to the reference dataset using the estimated motion. A flowchart illustrating the algorithm is shown in Fig.6. The pair of datasets to be registered are firstly transformed by the DT-$\mathbb{C}$WT and the levels which will be used for motion estimation are selected. The subband coefficients of the sensed dataset are shifted according to the motion
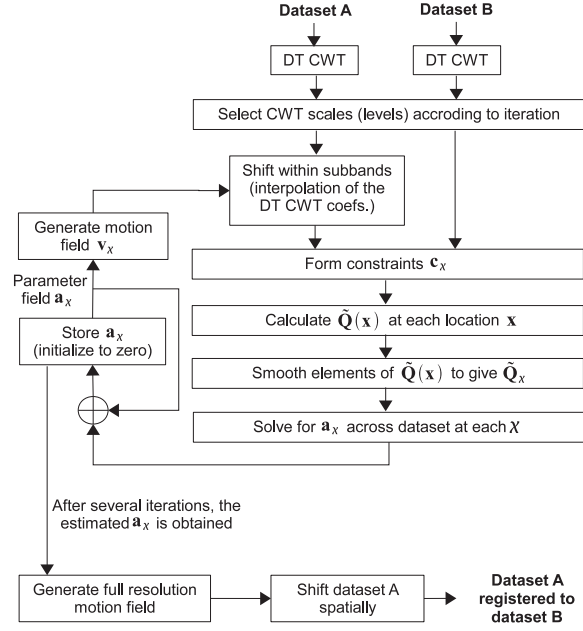
Fig. 6.   Flowchart of the image registration algorithm.

field produced by previous iterations. The shifted coefficients of the sensed dataset, together with the coefficients of reference dataset, are used to generate motion constraints. The $\tilde{\mathbf{Q}}(\mathbf{x})$ matrix can then be calculated at each location $\mathbf{x}$ and smoothed across each locality χ to give $\tilde{\mathbf{Q}}_{\chi}$. Next, the affine parameters which minimize the least squared error are obtained and added to the affine parameter estimates from previous iterations to generate the motion field. After all the iterations, the sensed dataset is finally interpolated in the 3-D spatial domain to register to the reference dataset. The main blocks within the algorithm will now be described.

A. DT-ℂWT on input datasets

The algorithm takes two 3-D datasets A and B as inputs, where B is the reference dataset and A is the sensed dataset. The two datasets are forward transformed with the 3-D DT-ℂWT and their complex wavelet coefficients at each level (except level 1, see section II-C) are obtained.

B. Select CWT scales (levels) according to iteration

The multi-resolution nature of the DT-ℂWT means that we can estimate the motion from different scales. For example, if we choose the complex wavelet coefficients at level 3 to perform motion estimation,

then each coefficient corresponds to a block of 8^3 voxels in the original dataset. This means one affine vector will be estimated for each of these 8^3 blocks.

It is important to realize that a wrong motion vector is likely to be produced if the phase change of a given complex wavelet coefficient exceeds the range $-\pi$ to $+\pi$, as this causes ambiguity for deciding the motion. For a given amount of motion, the phase change of coarser level complex coefficients will be smaller than that of finer level coefficients by a factor of 2 per scale level [28]. This shows that by using coarser level coefficients, the estimation algorithm can cope with larger motion, whilst with finer level coefficients it can only tackle small motion. However, performing motion estimation from coarser levels only may lead to inaccurate local motion estimates since the selected scale may be too coarse to capture all the important data features and the real local motion. This reveals a trade-off for selecting the levels at which the motion estimation should be performed: coarser level coefficients can estimate large motion but with limited accuracy, whilst finer level coefficients can give good local motion accuracy but cannot reliably estimate large motion vectors.

In order to achieve accurate motion estimation over a wide range, we adopt a coarse to fine approach to estimate the motion iteratively. In the first few iterations, the motion field should be estimated from coarse level coefficients only (to handle large motion) and this motion field is then used to shift the sensed dataset towards the reference. Once the large motion between the two datasets has been compensated, later iterations can focus on estimating the small local residual motion errors by using finer level coefficients. In this way the motion estimate is gradually refined to approach the true motion field.

C. Shift within subbands (interpolation of the DT-ℂWT coefficients)

The feasibility of interpolating DT-ℂWT coefficients within each subband separately relies on the transform's shift-invariant properties, as introduced in section II-A. The DT-ℂWT coefficients of dataset A need to be shifted and interpolated using estimated motion from previous iterations. After interpolation, the complex coefficients of dataset A should look more similar to those of dataset B because the amount of motion between A and B has been reduced. Finer level coefficients may then be used to perform motion estimation in the subsequent iterations.

One may argue that dataset A could be shifted with the estimated motion in the spatial domain and then transformed with the DT-ℂWT to get the wavelet coefficients for the shifted dataset. This method is feasible but tends to be slow since shifting a 3-D dataset is computationally demanding. The advantage of shifting in the complex wavelet domain is that it provides a fast and smooth way of aligning the datasets, as the number of DT-ℂWT coefficients at any level above 1 is much smaller than the sample size of the

original dataset, and the coefficients are well bandlimited. Moreover, the computations of performing the DT-$\mathbb{C}$WT are avoided within the iterative loop.

We must be aware that complex coefficients in each subband are bandpass signals and should not be interpolated in the normal way for lowpass signals. The DT-$\mathbb{C}$WT filters introduce a different phase offset rate to each of the subbands, and so direct interpolation will not produce the correct result. Our method for interpolating complex coefficients is as follows:

(1) De-rotate the phase of the bandpass complex coefficients to compensate for the phase offset rate and center the subband on zero frequency;

(2) Interpolate the real and imaginary parts of the de-rotated coefficients, using conventional (tri-)linear or cubic methods;

(3) Re-rotate the phase of the complex coefficients to restore their phase offset rate and to correct their bandpass center frequency.

The details of subband interpolation are discussed in appendix A.

D. Form constraints and calculate $\tilde{\mathbf{Q}}(\mathbf{x})$ at each location $\mathbf{x}$

The phase of the DT-$\mathbb{C}$WT coefficients can be used to form the constraints as described by (13). With the constraint vectors, we can then obtain the $\tilde{\mathbf{Q}}(\mathbf{x})$ matrix at each location $\mathbf{x}$ and at each chosen scale by using (19).

At each wavelet scale, the locations $\mathbf{x}$ are chosen to be at the centers of cubes bounded by 8 adjacent coefficients (the u_k and v_k of (14)). The derivatives of the column vector in (13) are then calculated by forming the two cubes of complex coefficients, $\mathbf{u}$ and $\mathbf{v}$, into corners of a 4-D hypercube, and by taking conjugate products across each pair of hyperfaces of the hypercube in turn. The 8 conjugate products from each hyperface-pair are then summed (similar to the summation in the numerator of (14), which is used for the $\frac{\partial \theta}{\partial t}$ term) and the phase of the complex resultant is the required phase derivative. Thus the derivatives are the average phase shifts at the center of each hypercube with respect to x, y, z and t, where the averages are effectively weighted by the magnitudes of the conjugate product terms so that large coefficient pairs contribute more to the phase 'average' than smaller pairs.

E. Smooth elements of $\tilde{\mathbf{Q}}(\mathbf{x})$ to give $\tilde{\mathbf{Q}}_\chi$

Recall that each motion constraint vector from (13) has a weighting factor $C_d(\mathbf{x})$ which reflects our confidence in the constraint. Equation (19) shows that a large weight motion constraint $\mathbf{c}_d(\mathbf{x})$ will

contribute more to the elements of $\tilde{\mathbf{Q}}(\mathbf{x})$ than a smaller one. Likewise in (20), larger $\tilde{\mathbf{Q}}(\mathbf{x})$ matrices will contribute more to $\tilde{\mathbf{Q}}_{\chi}$ than smaller ones for each locality χ.

However, it can be seen from (21) and (24) that when $\tilde{\mathbf{Q}}_{\chi}$ is used to solve for the affine vector $\mathbf{a}_{\chi}$, the solution will be independent of the total weight of $\tilde{\mathbf{Q}}_{\chi}$. In this way the weighting factors assigned to the motion constraints affect their relative contributions to the affine motion solution but the overall weight does not affect the final result. In smooth data regions or where there are no consistent features between datasets A and B, some or all of the eigenvalues of $\mathbf{Q}_{\chi}$ will be small and the resulting affine parameters will not be reliable.

A solution to this problem is to smooth the elements of the $\tilde{\mathbf{Q}}(\mathbf{x})$ matrices spatially across the dataset. The basic idea is to bring the motion information from locations with larger weight constraint vectors to those with smaller weight. This can be achieved by expanding each locality χ to include regions which overlap with other adjacent localities and by using a smoothly decaying weighting $w(\mathbf{x} - \boldsymbol{\chi}_0)$ as one moves away from $\boldsymbol{\chi}_0$, the center of χ. Hence (20) becomes

$$\tilde{\mathbf{Q}}_{\chi} = \sum_{\mathbf{x} \in \chi} w(\mathbf{x} - \boldsymbol{\chi}_0) \, \tilde{\mathbf{Q}}(\mathbf{x}) \tag{25}$$

and the localities χ are now larger and overlapping. This effectively applies a spatial low-pass smoothing filter, defined by the $w(\mathbf{x} - \boldsymbol{\chi}_0)$, to the $\tilde{\mathbf{Q}}(\mathbf{x})$ matrices. Typically there are many localities χ covering the whole dataset volume.

We find that a simple triangular low-pass filter gives good performance. The choice of the smoothing filter size (i.e. number of taps) is application dependent. A large filter should be used if the motion of the object is believed to be relatively smooth, i.e. the 12-element affine vectors are likely to be similar at nearby localities. However, if the motion varies in a significantly non-affine way across the dataset, then a small smoothing filter will be more desirable. It would be relatively easy to make the filter adaptive to the data, but we have not investigated this.

The filtering in (25) also allows easy combination of the $\tilde{\mathbf{Q}}(\mathbf{x})$ matrices across scale, where the basic sampling intervals of $\mathbf{x}$ are different. We use simple triangular filters to upsample or downsample the matrices from different scales so they all are sampled at the chosen grid for the localities χ. Typically the grid for χ corresponds to that for the level-3 or level-4 wavelet coefficients.

F. Solve for $\mathbf{a}_{\chi}$ and generate the motion field

The algorithm estimates the motion iteratively. Every iteration produces a set of affine vectors from (24), and they are added to the $\mathbf{a}_{\chi}$ estimated from previous iterations. As described in section IV-C, this

motion field is used to shift the DT-$\mathbb{C}$WT coefficients of the sensed dataset and the shifted coefficients are used for the next iteration of motion estimation.

The 3-D motion field is computed at the resolution and grid points of each wavelet scale that is being used, by linearly interpolating affine vectors from the nearest locality centers χ_0, and then by using the affine expression of (15) at each grid point. The multi-scale motion fields at the selected scales are finally passed to the block 'Shift within subbands' to complete the iterative loop.

G. Registration by spatial transform

After several iterations, a set of affine parameters are obtained which accurately describe the motion between the sensed and the reference datasets. The affine parameters are then up-sampled to produce the motion field at the full resolution, i.e. each voxel of the dataset has a corresponding motion vector. With this motion field, the sensed dataset can then be registered by interpolation in the 3-D spatial domain to align it with the reference dataset. An alternative method of registration would be to motion compensate every subband in the wavelet domain and then inverse transform the result, but this tends to introduce slight artifacts due to the transform being only approximately shift invariant. Furthermore it does not save any computation. Hence we recommend use of spatial domain interpolation to perform the final registration step.

V. DETAILS OF THE REGISTRATION ALGORITHM

This section includes in-depth discussions on some of the details of our algorithm.

A. Rigid body registration

The difference between rigid body and non-rigid body registration is that the motion of a rigid body always conforms to a single affine model (i.e. $\mathbf{a}_\chi$ must be the same at every locality of the dataset), whereas the motion of a non-rigid body is locally characterized. Thus for rigid body registration, the $\tilde{\mathbf{Q}}_\chi$ matrices at each locality should be the same. This implies, when estimating rigid motion, that the $\tilde{\mathbf{Q}}_\chi$ matrices at each locality can simply be averaged to produce a global $\tilde{\mathbf{Q}}$ which is denoted by $\tilde{\mathbf{Q}}_{\mathrm{mean}}$. Then $\tilde{\mathbf{Q}}_{\mathrm{mean}}$ replaces the original local $\tilde{\mathbf{Q}}_\chi$ matrix at all localities before solving for a single affine vector $\mathbf{a}_{\mathrm{mean}}$.

Even for non-rigid body registration, it can often be best to perform the first few iterations using the rigid body registration mode, before carrying out the non-rigid body motion estimation. This means that we start by registering the two datasets as a whole using coarse wavelet scales only to compensate for

possibly large motion, and then bring in local motion information on later iterations by switching to the non-rigid body mode and finer wavelet scales. Using rigid body mode additionally helps to reduce the chance of $\mathbf{Q}$ becoming ill conditioned, since it adopts the largest possible aperture (the whole image) for the purely coarse-level iterations, at which ill conditioning is most likely because of low spatial detail.

B. Selecting DT-$\mathbb{C}$WT levels for iterations

For every iteration, one or several levels of DT-$\mathbb{C}$WT can be selected to carry out motion estimation. The levels should be chosen in the sequence coarse to fine, in order to estimate the large components of motion first and then gradually refine the estimates. A typical choice of DT-$\mathbb{C}$WT levels ranges from level 5 or levels 5 and 4 in early iterations, to levels 4, 3 and 2 in the final few iterations, which take much longer to compute. There is a big computational gain from minimizing the number of iterations on which level 2 is used, as the number of constraint equations increases by a factor of 8 as each finer level is introduced.

It should be noted that the DT-$\mathbb{C}$WT in its simplest form requires the size of the dataset to be a multiple of 2^K in each dimension, where K is the coarsest transform level used. However the DT-$\mathbb{C}$WT can be modified slightly to break the restriction on size, by appending symmetrically extended (mirrored) coefficients as necessary at opposite edges of the LLL band after each level of transform, so as to ensure the size of the LLL band is always divisible by 8 in each dimension before it is passed to the next coarser level. The modified DT-$\mathbb{C}$WT only requires that the initial datasets be a multiple of 4 along each dimension. Some care must be taken, however, in the programming of the motion estimation parts of the algorithm to allow for the changes in subband sizes that this modification produces.

C. Motion estimation at dataset boundaries

In the DT-$\mathbb{C}$WT, to avoid boundary discontinuities the dataset is symmetrically extended along each of the dimensions before being filtered by the high-pass or low-pass filters. Although symmetric extension is a good technique for reducing edge effects, it leads to inaccuracy in estimating motion normal to the boundary of the dataset. This is because motion near the dataset boundary will cause reflected motion in the symmetrically extended region. The components of these two motions, normal to the boundary, move in opposite directions to each other and thus tend to result in poor motion estimation near boundaries.

Unfortunately it is not straightforward to estimate accurately the motion at dataset boundaries. To reduce the estimation error, we recommend using motion information at inner localities to infer motion at the boundary localities. This scheme can simply be achieved by zeroing out some or all of the motion

constraint vectors at the boundary localities when the constraints are generated. This is equivalent to saying that there is no information about certain components of motion at the boundary localities. If all motion constraints near the dataset boundaries are set to zero, $\tilde{\mathbf{Q}}(\mathbf{x})$ will also be zero at these boundary localities. When the $\tilde{\mathbf{Q}}(\mathbf{x})$ matrices are smoothed across the localities as described in section IV-E, the information of the $\tilde{\mathbf{Q}}(\mathbf{x})$ matrices at neighboring inner localities will leak into the $\tilde{\mathbf{Q}}_\chi$ near the boundaries. In this way, the affine motion models at the boundaries will be extrapolated from the affine models of the inner regions.

D. Modification to the $\mathbf{Q}_\chi$ matrix

We have shown in equation (24) that the optimal affine parameter vector solution is $\mathbf{a}_\chi = -\mathbf{Q}_\chi^{-1}\mathbf{q}_\chi$. However in practice, the $\mathbf{Q}_\chi$ at some localities may be found to be near singular (very ill-conditioned). This is undesirable because small numerical errors in $\mathbf{Q}_\chi$ will lead to large inaccuracies in the solution of $\mathbf{a}_\chi$. The ill-conditioning of $\mathbf{Q}_\chi$ implies that the 12-parameter affine model is over-fitting the local motion. The source of the ill-conditioning is often due to the local data content being relatively simple and so the local motion can be described by fewer than 12 parameters. To remedy this problem (often known as the aperture problem), one possible solution is to use a large smoothing filter when the $\tilde{\mathbf{Q}}_\chi$ matrices are calculated. However, applying a large filter may result inaccurate local motion estimation. A solution, which we have used successfully with relatively rigid brain scans, is to modify $\tilde{\mathbf{Q}}_\chi$ slightly to become $\tilde{\mathbf{Q}}'_\chi$, where

$$\tilde{\mathbf{Q}}'_\chi = \tilde{\mathbf{Q}}_\chi + \lambda\tilde{\mathbf{Q}}_{\mathrm{mean}} \tag{26}$$

Recall that $\tilde{\mathbf{Q}}_{\mathrm{mean}}$ is the mean of $\tilde{\mathbf{Q}}_\chi$ over all localities, i.e. $\tilde{\mathbf{Q}}_{\mathrm{mean}}$ represents the estimate of the global motion. λ in (26) should be a small constant which we will discuss shortly. With the definition of $\tilde{\mathbf{Q}}'_\chi$ in (26), the solution of the affine parameters is now expressed as follows:

$$\mathbf{a}_\chi = -\tilde{\mathbf{Q}}'^{-1}_\chi\mathbf{q}'_\chi \tag{27}$$

where $\mathbf{Q}'_\chi$ and $\mathbf{q}'_\chi$ come from the newly defined $\tilde{\mathbf{Q}}'_\chi$:

$$\tilde{\mathbf{Q}}'_\chi = \begin{bmatrix} \mathbf{Q}'_\chi & \mathbf{q}'_\chi \\ \mathbf{q}'^{\mathrm{T}}_\chi & q'_{0\chi} \end{bmatrix} \tag{28}$$

The modified $\tilde{\mathbf{Q}}'_\chi$ can be regarded as the superposition of the local motion and a small fraction of global motion. This is equivalent to driving the local motion estimate slightly towards the global motion

and the amount is controlled by λ. The value of λ is not critical and we express it as:

$$\lambda = \sqrt{\frac{0.001 \cdot \sum_{\text{all } \chi} \text{Energy of } \tilde{\mathbf{Q}}_\chi}{(\text{\# of localities}) \, (\text{Energy of } \tilde{\mathbf{Q}}_{\text{mean}})}} \qquad (29)$$

where the energy of a matrix is defined as the sum of all its elements squared. It is best to consider the meaning of $\lambda \tilde{\mathbf{Q}}_{\text{mean}}$ in order to interpret λ in the above equation. With the definition of λ in (29), the energy of $\lambda \tilde{\mathbf{Q}}_{\text{mean}}$ is just 0.001 of the mean energy of the $\tilde{\mathbf{Q}}_\chi$.

With the small amount of added global motion, $\tilde{\mathbf{Q}}'_\chi$ no longer tends to be singular. This technique also tends to give a more regularized motion field, especially in regions where the motion is ill-defined.

For example, consider typical medical images with human organs in the center being surrounded by dark backgrounds. The featureless background is usually not perfectly dark and some noise exists in these regions. Our motion estimation gives a small weighting factor to the dark backgrounds, but at the localities far away from the features it will still try to register the noise because motion from the feature-rich regions is not smoothed enough to affect these far away localities. However, with the modified $\tilde{\mathbf{Q}}'_\chi$, a small amount of global motion is added to every locality, and so it will tend to suppress noisy motion estimates in the background localities and make them look like the global motion. Note that although the motion estimates at the featureless background are not critically important, it is best to stop them from being irregular and introducing artifacts. This can have the added advantage of speeding up the slice-based 3-D spatial interpolation which follows the motion estimation.

VI. EXPERIMENTAL RESULTS

In this section, we show that our algorithm gives highly accurate estimation of motion on artificial and real-world datasets. The medical datasets in sections VI-B and VI-C, together with the Matlab scripts for visualizing datasets, are available online [1].

A. Registration of synthetically shifted datasets

An artificial 3-D shell pattern is generated as shown in Fig.7a. It is produced by stacking several cubical shells together and warping them with a non-rigid motion field. The shape of the cubical shell is designed like this for two reasons: 1. its asymmetric nature avoids ambiguity when analyzing the rotation components; 2. the rather irregular spatial features excite all the DT-$\mathbb{C}$WT subbands so we can test the motion estimates from all subbands.
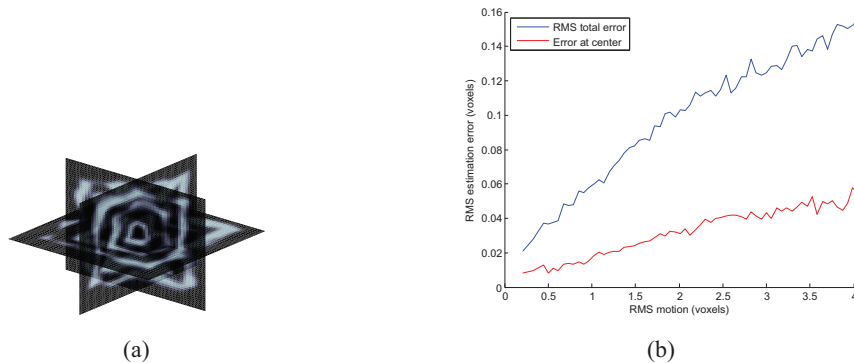
---

[1]http://mars3.stanford.edu/hchen/imagereg.zip

Fig. 7. (a) The intersection view of the 3-D shell pattern ($64 \times 64 \times 64$). (b) The rms motion estimation error versus the rms value of the true motion.

The synthetic 3-D shell pattern is warped by a single random affine motion. The motion between the original and the warped datasets is estimated and compared with the true motion. We have used translation, rotation, scaling and shear components to produce true affine motion. The affine parameters are randomly generated from zero mean Gaussian distributions (except for the scaling component distribution, whose mean is set to one). In order for all types of motion component to contribute almost equally to the combined motion, the rotation, scaling and shear components are scaled such that their motion at a radius of $\frac{n}{4}$ (where n is the linear size of the n^3 dataset) from the center is approximately equal to the translation motion.

To evaluate the accuracy of our registration algorithm, we follow the evaluation method as described in [21], where the estimated motion RMS error is plotted against the ground truth motion RMS value. To get a statistical measure of the registration accuracy, the registration results are averaged over a large number of experiments. The error curve plotted in Fig.7b shows that our algorithm achieves very high accuracy.

We have also performed experiments to evaluate the algorithm performance on a real MRI dataset of the human brain, as shown in Fig.8a. The testing conditions are the same as those of the synthetic 3-D shell pattern and the results are shown in Fig.8b. Comparing with Hemmendorff's method [21] on the same dataset, our method achieves better accuracy and lower filter computational complexity. As shown in Appendix B, the DT-ℂWT requires 75 operations per voxel compared to Hemmendorff's method which requires 310 operations per voxel.
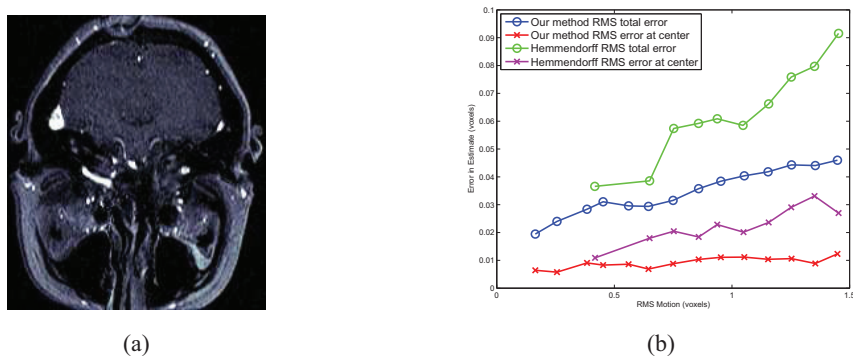
(a)   (b)

Fig. 8.   (a) The MRI dataset ($140 \times 140 \times 68$, 2mm slice sampling spacing). (b) The rms motion estimation error versus the rms value of the true motion. Our rms error curves are generated using 250 experimental results, while Hemmendorff's error curves are generated using the 124 data points presented in Fig. 7 of [21].
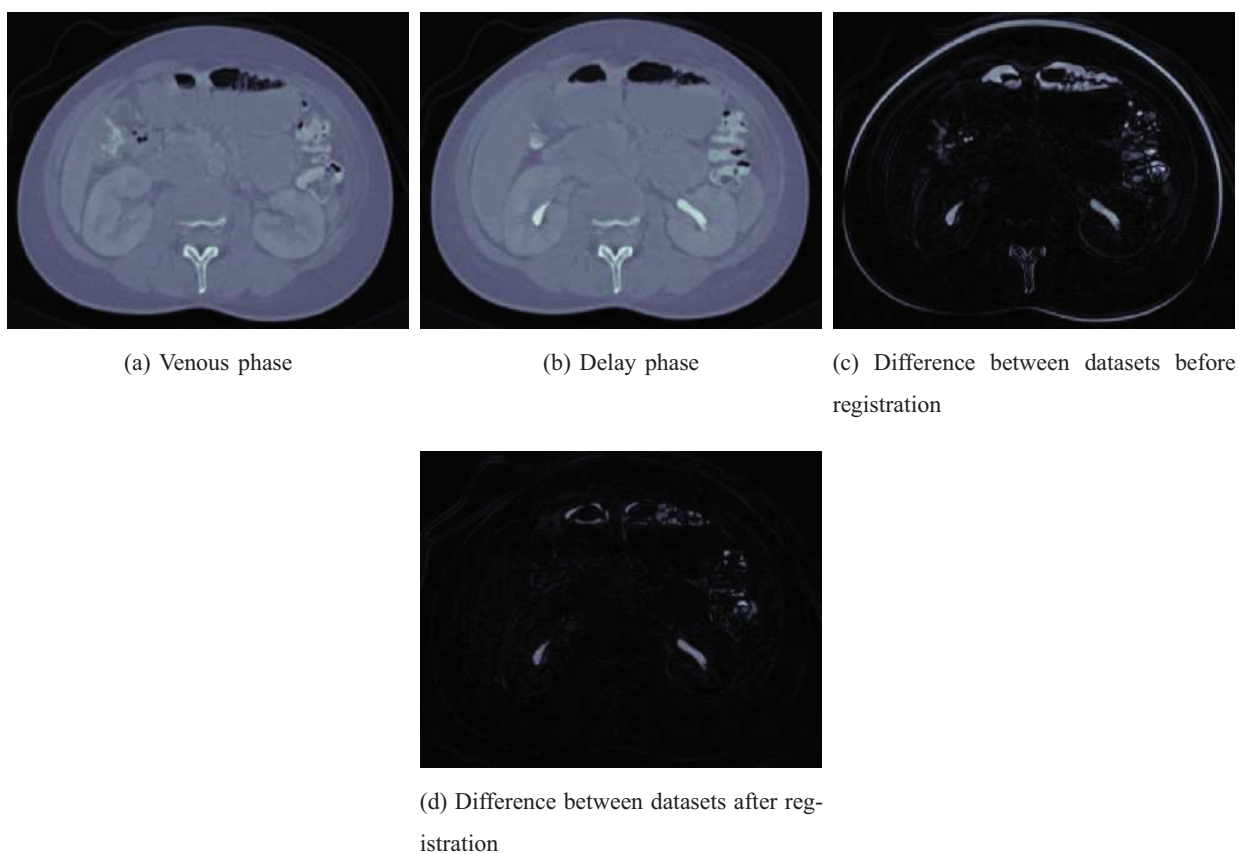

(a) Venous phase   (b) Delay phase   (c) Difference between datasets before registration

(d) Difference between datasets after registration

Fig. 9.   Registration of 3-D CT scans ($384 \times 512 \times 128$) with contrast agent, where the venous phase dataset is being registered to the delay phase dataset. The registration is performed in 3-D, but only a single slice is displayed here for the convenience of visualization.

B. Registration of 3-D CT scans with contrast agent

In medical radiology, contrast agent injection techniques are commonly used to improve the visibility of internal body structures. Two 3-D abdominal CT scans (Fig.9a and Fig.9b) are acquired during the venous phase and the delay phase of kidney contrast agent injection. There is an interval of a few minutes between the acquisition of the two scans and motion has occurred mainly due to patient movement and breathing. To show the effect of image registration, subtraction is performed on the datasets before and after registration. Before registration, the motion artifacts can be easily visualized in Fig.9c. We then apply our algorithm to align the venous phase dataset with the delay phase dataset and the difference after registration is shown by Fig.9d. Comparing Fig.9c and Fig.9d, it can be seen that the effects of motion at the outer boundary and the backbone regions are largely eliminated. On the other hand, the contrast agent in the kidneys as well as the gases in the stomach and the intestines are shown clearly. These observations are expected since the differences in these regions are not related to motion.

C. Registration of MRI datasets

Fig.10 shows the registration of paired MRI scans taken before and after the operation on a brain pituitary tumor. The middle part of the tumor was debulked during the operation but the right part was left alone. In this scenario, the objects in the two 3-D MRI datasets are not the same since the tumor region has changed. Recall that we use weighted motion constraints to address the problem of registering non-identical objects, as described in section III-B1. The weighting factor of the motion constraint is small when the image features are dissimilar in the two datasets, which occurs in the middle tumor region where the features cannot be well matched. In Fig.10, it can be seen that, apart from the middle tumor (in the red boxes), the other parts of the post-operative dataset are well aligned with the pre-operative dataset.

VII. CONCLUSIONS

We have shown how to perform accurate 3-D registration using the phase information of the DT-$\mathbb{C}$WT. Our algorithm adopts an efficient iterative coarse-to-fine approach which estimates large motion first and then refines the motion field. It relies on shift-invariance and good directional filtering properties, which are key features of the DT-$\mathbb{C}$WT. Non-rigid motion is well modelled by a locally affine parametric model, whose parameters are obtained by minimizing the squared errors of the model. The weighting factors of the motion constraints are designed to reduce perturbations of the motion estimates due to inconsistent
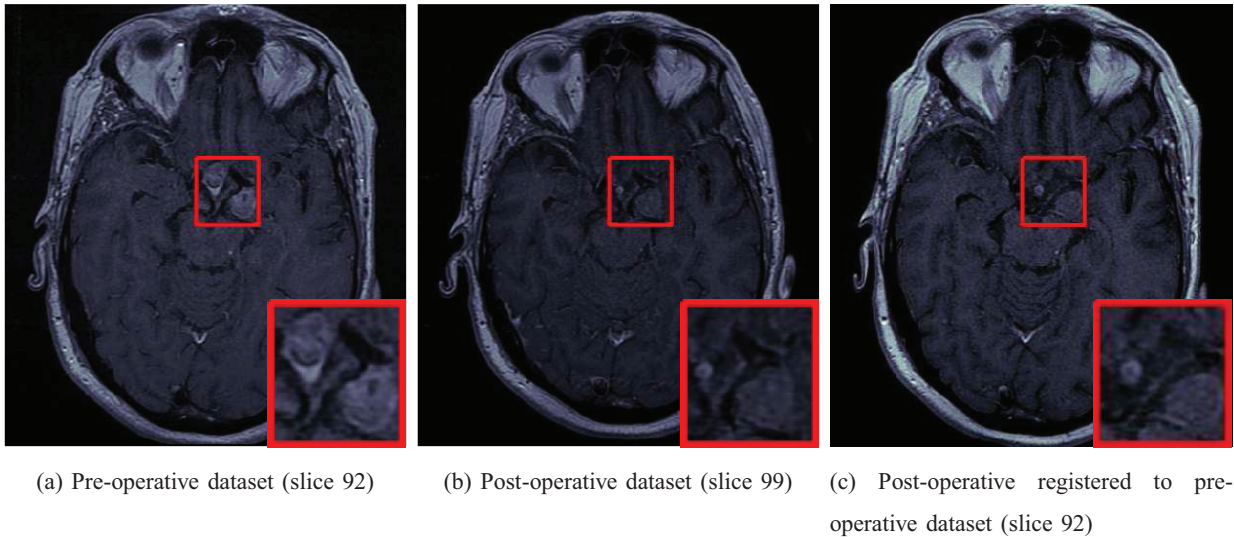
(a) Pre-operative dataset (slice 92)   (b) Post-operative dataset (slice 99)   (c) Post-operative registered to pre-operative dataset (slice 92)

Fig. 10.   Registration of 3-D MRI scans ($512 \times 512 \times 128$) before and after operation. The tumor region in each MRI image is highlighted by the red boxes.

features and noise. From the final estimated motion field, the sensed dataset can be accurately registered to the reference dataset by spatial-domain interpolation.

APPENDIX A
INTERPOLATION OF DT-$\mathbb{C}$WT COEFFICIENTS

The DT-$\mathbb{C}$WT coefficients cannot be directly interpolated since the transform produces bandpass filters which introduce a relatively high phase rotation rate to the coefficients [1]. In order to center the pass-band of the DT-$\mathbb{C}$WT subband outputs on zero frequency, we set up the expected rotation rate for each subband to correspond to a frequency offset of $-\frac{1}{4}$ and $-\frac{3}{4}$ times the subband output sampling rate, which are the expected rotation rates for the low-pass and the high-pass filters respectively.

Note that $-\frac{1}{4}$ of the sampling frequency gives a phase increment of $-\frac{\pi}{2}$ between samples. Nevertheless in practice, we reduce this value a little to $-\frac{\pi}{2.1}$, to model better the slight asymmetry of the scaling function and wavelet frequency responses. For ease of demonstration, denote $\omega_0 = -\frac{\pi}{2.1}$ and $\omega_1 = -\frac{3\pi}{2.1}$. The expected phase rotation rate for each of the 28 subbands can simply be calculated from the subband's corresponding filtering process. The rule is that high-pass (H), low-pass (L), conjugate high-pass (H*) and conjugate low-pass (L*) correspond to phase rotations of ω_1, ω_0, $-\omega_1$ and $-\omega_0$ respectively. For example, for the H*LL band (remembering this means conjugate high-pass filtering on rows, and low-pass filtering on columns and slices), the expected phase rotation is $-\omega_1$, ω_0 and ω_0 in the x, y and z

directions respectively.

For each selected subband, having obtained the expected phase rotation rate, the DT-$\mathbb{C}$WT coefficients are de-rotated by multiplying by phase rotation terms

$$\exp[-j\omega_x k_x - j\omega_y k_y - j\omega_z k_z]$$

where k_x, k_y and k_z are the linear indices of the coefficients along the x, y and z directions; and ω_x, ω_y and ω_z are the expected phase rotation rates in these directions introduced by the H or L filtering processes of the subband.

Interpolation of the de-rotated subband coefficients can now be performed to shift the subband. Finally the interpolated coefficients must be rotated back by multiplying them by

$$\exp[j\omega_x(k_x + v_x) + j\omega_y(k_y + v_y) + j\omega_z(k_z + v_z)]$$

where v_x, v_y and v_z are the motion components in the x, y and z directions respectively.

APPENDIX B
ALGORITHM COMPLEXITY

Assuming the input 3-D dataset is of the size N^3. Performing a 1-D filtering on this dataset with a filter of length h requires $N^3 h$ operations, where 1 operation = 1 addition + 1 multiplication. For DT-$\mathbb{C}$WT filtering, we use $h = 9$-tap filter for level 1 and $m = 14$-tap filter for higher levels as presented in [1]. Since we only keep the LLL band in the level 1 decomposition (as described in Section II-C), performing level 1 DT-$\mathbb{C}$WT needs $3N^3 h$ operations on 3 dimensions. Level 2 requires $3N^3 m$ operations, and DT-$\mathbb{C}$WT in each higher level requires $\frac{1}{8}$ of the operations of the previous level, since the filter output from the previous level is downsampled by 2 in each dimension. Consequently,

$$\text{DT-}\mathbb{C}\text{WT complexity} = 3N^3 h + 3N^3 m (1 + \frac{1}{8} + \frac{1}{64} + \cdots)$$

$$= 75N^3 \text{ operations}$$

We perform similar analysis on the filter bank used in Hemmendorff's algorithm. Referring to Fig. 4 of [21], each 9-tap real-valued lowpass filter requires $9N^3$ operations, while each 9-tap complex-valued quadrature filter requires $18N^3$ operations since it needs $9N^3$ for the real part and $9N^3$ for the imaginary part. Therefore, the complexity for level 1 decomposition as illustrated in Fig. 4 of [21] is $(9 \times 12 + 18 \times 9)N^3 = 270N^3$. To create a multiscale tree, an extra lowpass filter is needed in the final

step of the level 1 decomposition to generate a LLL band. The LLL band can then be downsampled by 2 in each dimension so the next level of filtering requires $\frac{1}{8}$ of the operations of the previous level. Hence,

$$[21] \quad \text{complexity} = [270 + (9 + 270) \times (\frac{1}{8} + \frac{1}{64} + \cdots)]N^3$$

$$\simeq 310N^3 \text{ operations}$$

REFERENCES

[1] N. G. Kingsbury, "Complex wavelets for shift invariant analysis and filtering of signals," *Journal of Applied and Computational Harmonic Analysis*, vol. 10, no. 3, pp. 234–253, 2001.

[2] J. Matas, O. Chum, M. Urban, and T. Pajdla, "Robust wide-baseline stereo from maximally stable extremal regions," *Image and Vision Computing*, vol. 22, no. 10, pp. 761 – 767, 2004.

[3] H. Li, B. S. Manjunath, and S. K. Mitra, "A contour-based approach to multisensor image registration," *IEEE Transactions on Image Processing*, vol. 4, no. 3, pp. 320 –334, Mar. 1995.

[4] G. Takacs, V. Chandrasekhar, S. Tsai, D. Chen, R. Grzeszczuk, and B. Girod, "Unified real-time tracking and recognition with rotation-invariant fast features," in *Proceedings of IEEE Conference on Computer Vision and Pattern Recognition*, 2010, pp. 934–941.

[5] E. Rosten, R. Porter, and T. Drummond, "Faster and better: A machine learning approach to corner detection," *IEEE Transactions Pattern Analysis and Machine Intelligence*, vol. 32, pp. 105–119, 2010.

[6] D. Ta, W. Chen, N. Gelfand, and K. Pulli, "Surftrac: Efficient tracking and continuous object recognition using local feature descriptors," in *Proceedings of IEEE Conference on Computer Vision and Pattern Recognition*, 2009.

[7] R. Berthilsson, "Affine correlation," in *International Conference on Pattern Recognition*, vol. 2, Aug. 1998, pp. 1458 –1460.

[8] A. Simper, "Correcting general band-to-band misregistrations," in *International Conference on Image Processing*, Sep. 1996, pp. 597 –600.

[9] G. Wolberg and S. Zokai, "Image registration for perspective deformation recovery," in *SPIE International Symposium on Aerospace, Defense Sensing, Simulation, and Controls*, 2000, p. 12.

[10] P. Viola and W. M. Wells III, "Alignment by maximization of mutual information," *International Journal of Computer Vision*, vol. 24, pp. 137–154, 1997.

[11] F. Macs, A. Collignon, D. Vandermeulen, G. Marchal, and P. Suetens, "Multimodality image registration by maximization of mutual information," *IEEE Transactions on Medical Imaging*, vol. 16, pp. 187–198, 1997.

[12] P. Thevenaz and M. Unser, "An efficient mutual information optimizer for multiresolution image registration," in *International Conference on Image Processing*, vol. 1, Oct. 1998, pp. 833 –837.

[13] C. Studholme, D. L. G. Hill, and D. J. Hawkes, "An overlap invariant entropy measure of 3d medical image alignment," *Pattern Recognition*, vol. 32, no. 1, pp. 71 – 86, 1999.

[14] P. A. Van Den Elsen, E. J. D. Pol, and M. A. Viergever, "Medical image matching - a review with classification," *IEEE Engineering in Medicine and Biology Magazine*, vol. 12, pp. 26–39, 1993.

[15] J. B. A. Maintz and M. A. Viergever, "A survey of medical image registration," *Medical Image Analysis*, vol. 2, no. 1, pp. 1–36, 1998.

[16] L. Brown, "A survey of image registration techniques," *ACM Computing Surveys*, vol. 24, no. 4, pp. 325–376, 1992.

[17] J. M. Fitzpatrick, D. L. G. Hill, and C. R. Maurer Jr., "Image registration," in *Handbook of Medical Imaging, Volume2: Medical Image Processing and Analysis*. SPIE, 2000, pp. 447–513.

[18] B. Zitová and J. Flusser, "Image registration methods: a survey," *Image and Vision Computing*, vol. 21, pp. 977–1000, 2003.

[19] A. Gholipour, N. Kehtarnavaz, R. Briggs, M. Devous, and K. Gopinath, "Brain functional localization: A survey of image registration techniques," *IEEE Transactions on Medical Imaging*, vol. 26, pp. 427–451, 2007.

[20] M. Hemmendorff, "Motion estimation and compensation in medical imaging," Ph.D. dissertation, Department of Biomedical Engineering, Linköpings universitet, SE-581 85 Linköping, Sweden, 2001.

[21] M. Hemmendorff, M. T. Andersson, T. Kronander, and H. Kuntsson, "Phase-based multidimensional volume registration," *IEEE Transactions on Medical Imaging*, vol. 21, no. 12, Dec. 2002.

[22] I. W. Selesnick, R. G. Baraniuk, and N. G. Kingsbury, "The dual-tree complex wavelet transform," *IEEE Signal Processing Magazine*, vol. 22, no. 6, pp. 123–151, Nov. 2005.

[23] N. G. Kingsbury, "The dual-tree complex wavelet transform: a new technique for shift invariance and directional filters," in *IEEE Digital Singal Processing Workshop*, 1998.

[24] E. P. Simoncelli, W. T. Freeman, E. H. Adelson, and D. J. Heeger, "Shiftable multiscale transforms," *IEEE Transactions on Information Theory*, vol. 38, no. 2, pp. 587–607, 1992.

[25] R. Szeliski, "Image alignment and stitching: a tutorial," *Foundation and Trends in Computer Graphics and Vision*, vol. 2, pp. 1–104, Jan. 2006.

[26] T. Poggio, V. Torre, and C. Koch, "Computational vision and regularization theory," *Nature*, vol. 317, pp. 314–419, 1985.

[27] B. K. P. Horn and B. G. Schunck, "Determining optical flow," *Artificial Intelligence*, vol. 17, pp. 185–204, 1981.

[28] J. F. A. Magarey and N. G. Kingsbury, "Motion estimation using a complex-valued wavelet transform," *IEEE Transactions on Signal Processing*, vol. 46, no. 4, pp. 1069–84, 1998.

Huizhong Chen received the B.A. and M.Eng. degrees in electrical and information sciences, both from University of Cambridge, UK, in 2008 and 2009. As a recipient of the Kodak Fellowship, he is currently pursuing a Ph.D degree in Electrical Engineering at Stanford University, US. His current research interest is mobile visual search. He worked in the Signal Processing and Communications Laboratory at Cambridge University during his master's study, focusing on the applications of dual-tree complex wavelets. He also has past research experience on nanotube fabrication in the Nanomaterials Group at Cambridge.

Nick Kingsbury received the honours degree in 1970 and the Ph.D. degree in 1974, both in electrical engineering, from the University of Cambridge. He is a member of the IEEE.

From 1973 to 1983 he was a Design Engineer and subsequently a Group Leader with Marconi Space and Defence Systems, Portsmouth, England, specializing in digital signal processing and coding, as applied to speech coders, spread spectrum satcomms, and advanced radio systems. Since 1983 he has been a Lecturer in Communications Systems and Image Processing at the University of Cambridge and a Fellow of Trinity College, Cambridge. He was appointed to a Readership in Signal Processing at Cambridge in 2000, and to the position of Professor of Signal Processing in 2007. He is currently head of the Signal Processing and Communications Research Group.

His current research interests include image analysis and enhancement techniques, object recognition, motion analysis and registration methods. He has developed the dual-tree complex wavelet transform and is especially interested in the application of complex wavelets and related multiscale and multiresolution methods to the analysis of images and 3-D datasets.